11th International Symposium on Turbulence and Shear Flow Phenomena (TSFP11)
Southampton, UK, July 30 to August 2, 2019

TIME-RESOLVED TOPOLOGY OF SKIN-FRICTION LINES OVER AN AIRFOIL WITH TRAILING-EDGE SEPARATION

Austin Ma

Department of Mechanical Engineering
University of Alberta
Edmonton, AB
ama2@ualberta.ca

Bradley Gibeau

Department of Mechanical Engineering
University of Alberta
Edmonton, AB
bgibeau@ualberta.ca

Sina Ghaemi

Department of Mechanical Engineering
University of Alberta
Edmonton, AB
ghaemi@ualberta.ca

ABSTRACT

Time-resolved particle image velocimetry (PIV) was performed over a wall-parallel plane to investigate the unsteady near-wall topology of trailing-edge separation. The flow is a three-dimensional (3D) separation caused by an adverse pressure gradient (APG), which was formed on the aft section of a modified NACA 4418 airfoil. PIV was also conducted on a streamwise-wall-normal plane along the mid-span at separation, and the results are similar to previous studies of two-dimensional separation. The mean skin-friction lines obtained from the wall-parallel PIV showed a saddle point near mid-span and a pair of counter-rotating foci, forming what is known as a stall cell. Spectral analysis performed on the near-wall flow revealed that the flow contained mostly low-frequency motions. Saddle points and foci were difficult to observe in the instantaneous snapshots of the skin-friction lines due to small-scale turbulence. A low-pass filter was applied on the time-resolved images to investigate the low-frequency motions identified in the frequency spectrum. Investigation of the time-resolved snapshots revealed that foci are formed at high-shear regions created by an influx of local streamwise momentum from the upstream flow or backflow regions. The formation and dissipation of saddle points and foci due to streaks of strong local flow contribute to the intermittency of the separation line.

INTRODUCTION

The separation of a turbulent-boundary layer at the trailing edge of an airfoil is caused by an APG, and result in increased drag and decreased lift. Understanding the mechanics of flow separation allows engineers to develop new methods to delay or prevent separation, thus improving the performance of high-lift devices. The topology of 3D separated flow is studied by analysing the critical points present in the skin-friction pattern: saddle points, foci, and nodes. The flow is separated if it contains at least one saddle point in its skin-friction pattern (Tobak and Peake, 1982). The skin-friction pattern and flow topology exhibited on a stalled airfoil is dependent on the type of stall, aspect ratio, trip wire, and surrounding boundary condition (Broeren and Bragg, 2001; Liu *et al*., 2011; Dell'Orso and Amitay, 2018). The present paper focuses on an "owl-faced" pattern, defined as stall cells (Winkelmann and Barlow, 1980; Broeren and Bragg, 2001; Manolesos *et al*., 2014). The skin-friction pattern of a stall cell contains a saddle point accompanied with a pair of counter-rotating foci in the mean surface pattern (Manolesos *et al*., 2014).

Majority of the previous experimental studies conducted on stall cells were performed using fine tufts (Yon and Katz, 1998), oil flow visualization (Winkelmann and Barlow, 1980; Dell'Orso and Amitay, 2018) or low frame-rate PIV (Manolesos and Voutsinas, 2014; Dell'Orso and Amitay, 2018), which reveal limited information on the unsteady behaviour of stall cells. Broeren and Bragg (2001) linked stall cells to the low-frequency phenomenon observed by Zaman *et al*. (1985), which they attributed to an instability between a stalled and unstalled state. The low frequency phenomenon contained a non-dimensionalized frequency (Strouhal number) in the range of St = 0.02 to 0.05 ($St = f\,c\,\sin\alpha/U_\infty$), which is lower than the bluff body shedding frequency of 0.2.

The objective of this study is to describe the unsteady near-wall topology of an airfoil experiencing trailing-edge separation using time-resolved PIV. Time-resolved PIV will provide insight into the formation and evolution of separation structures (saddle points and foci) and its relationship to surrounding flow conditions. The results can provide guidelines for control of an intermittent trailing-edge separation over thick airfoils.

EXPERIMENTAL SETUP

Separation of a turbulent boundary layer due to an APG was formed over the aft section of a modified NACA 4418 airfoil at an angle-of-attack of 9.0º. The airfoil has a chord length of c = 975 mm and a span of s = 1170 mm as shown in figure 1. The profile was customized to have a flat rear section, which extended from 0.67c to the trailing-edge and a trip wire was placed at 0.2c. The experiments were performed inside a closed-loop wind tunnel with cross section of 2.4 × 1.2 m^2 ($W \times H$) at a freestream speed of U_∞ = 12.0 ms^{-1}, corresponding to a Reynolds number of Re_c = 750000. The origin is defined so that x = 0 is aligned with the most upstream point of zero mean velocity, y = 0 is the surface of the airfoil, and z = 0 is mid-span. The parameters U, V, and W presented in this article are defined as the instantaneous velocity in the x, y, and z-directions, respectively, while u, v and w are the fluctuating velocity components.

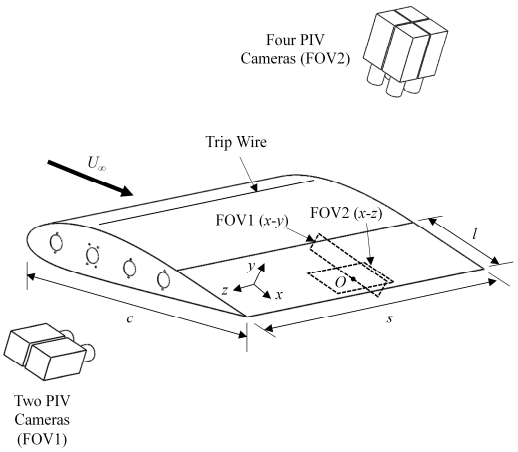

Figure 1. A schematic of the experimental setup highlighting field-of-view, coordinate system, and positions of cameras. The origin (O) of the coordinate system is located at the separation point at mid-span and 140 mm (0.14c) upstream of the trailing edge.

PARTICLE IMAGE VELOCIMETRY IN THE X-Y PLANE

The characteristics of the boundary layer at mid-span were investigated using planar PIV at the field-of-view (FOV) labelled as FOV1 in figure 1. A fog generator was used to generate 1 µm droplets as flow tracers. The tracers in the FOV were illuminated using a dual-head Nd:YLF laser (Photonics Industries DM20-527-DH), which is capable of outputting 527 nm light at 40 mJ per pulse with a pulse width of 170 ns at 1000 Hz. The laser was shaped into a 1 mm thick sheet using a combination of cylindrical lens and spherical lens. Two coated mirrors were used to direct the laser sheet orthogonally onto the airfoil along the mid-span. The flow was recorded using two high-speed cameras (Phantom v611) with a maximum resolution of 1280 × 800 pixels. The cameras contain a complementary metal oxide semiconductor (CMOS) sensor with 20 × 20 µm^2 pixels. Both cameras were fitted with 105 mm Sigma lenses set to an aperture setting of f/2, and placed 750 mm away from the viewing plane. The setup was calibrated and converted to physical dimension by imaging a calibration plate.

Double-framed images were collected at 24 Hz with a delay of 150 µs between adjacent frames. The experiment was repeated five times and each set of data contained 2700 images acquired over 112 s. Image and vector processing was performed on DaVis 8.4 (LaVision GmbH). In order to remove the background noise from the images, the ensemble minimum was subtracted from all of the images. Normalization of the particle intensities was accomplished by dividing the intensity values by the ensemble average. All images were cross-correlated multiple times with a final interrogation window size of 32 × 32 pixels with 75% overlap. The images were processed a second time using a sum-of-correlation method with a final window size of 8 × 8 pixels and 75% overlap (Meinhart *et al.*, 2000). The sum-of-correlation method allowed for smaller interrogation windows, resulting in a higher spatial resolution for the mean velocity field, which was desired for characterizing the near-wall portion of the boundary layer. After stitching the resultant vector fields and removing the unwanted boarders, the size of the FOV was (Δx, Δy) = 325 × 53 mm^2 with a digital resolution of 7.1 pix mm^{-1}.

PARTICLE IMAGE VELOCIMETRY IN THE X-Z PLANE

The near surface flow in vicinity of separation was measured using planar PIV at the FOV denoted as FOV2 in figure 1. The identical laser and Phantom v611 cameras were also used in this setup. Laser optics were used to collimate the laser beam into a 1.5 mm thick laser sheet and directed by a large mirror to be parallel with the surface of the model. The edge of the laser sheet was 2 mm away from the flat surface of the airfoil. Four cameras were used to increase the size of the viewing region and each camera was fitted with a 200 mm Nikon lens with an aperture setting of f/4 and extension rings. The front of the lens was positioned 1550 mm from the region of interest. Due to the physical size of the cameras, they were angled slightly in order to obtain a 15 mm overlap in the streamwise direction and 25 mm overlap in the spanwise direction. Because the angle was less than 1.0º, the parallax error introduced by tilting the cameras is less than 0.1%. After stitching the images and removing the unwanted edges, the effective FOV was (Δx, Δz) = 180 × 230 mm^2 with a digital resolution of 7.9 pix mm^{-1}.

Two different camera settings were utilized for capturing images within FOV2: one to obtain a large quantity of uncorrelated vector fields and another to gather time-resolved data. The two settings led to (*i*) eight single-frame images at 1750 Hz every second for 60 seconds, and (*ii*) 5000 single-frame images at 1750 Hz. The images obtained from the first configuration will be referred to as the cyclic data while the latter will be denoted as the time-resolved data. Collecting images in a cyclic configuration allowed for a longer sampling duration and uncorrelated vector fields between cycles, which were ideal for statistical analysis. By taking images at a high temporal rate within each cycle, a sliding-average correlation can be employed for the evaluation of the velocity vectors. This method increases the signal-to-noise ratio and is beneficial for measurements close to the wall, where particle displacement is small (Ghaemi *et al.*, 2012). The experiment was repeated 20 times for the cyclic configuration and five times for the time-resolved configuration.

All image and vector processing was performed using DaVis 8.4 (LaVision GmbH) once again. For the temporally resolved data, the images were processed similarly to the procedure outlined for FOV1. Background noise was removed by subtracting the ensemble minimum and then normalization was achieved by dividing the intensity values by the ensemble average. For the cyclic images, the ensemble average was subtracted from the images to remove background noise and achieve normalization. All images were cross-correlated using a sliding sum-of-correlation (Ghaemi *et al.*, 2012) with a kernel size of 2. Multiple passes were used with a final interrogation window size of 48 × 48 pixels and 75% overlap.

TURBULENT BOUNDARY LAYER

The progression of the boundary layer profile with chordwise distance within FOV1 is shown in figure 2. The streamwise coordinate (x) was normalized by the chord length of the airfoil (c) and the wall-normal coordinate (y) was normalized by the boundary layer thickness (δ_{99}) obtained at x/c = −0.15. The vectors are downsampled by a factor of six in the y-direction to improve visualization. Contours of the normalized mean velocity ($\langle U \rangle / U_\infty$) are shown in the background. The dashed line indicate where the mean streamwise velocity is zero. The mean flow separation is evident from the detachment of the boundary

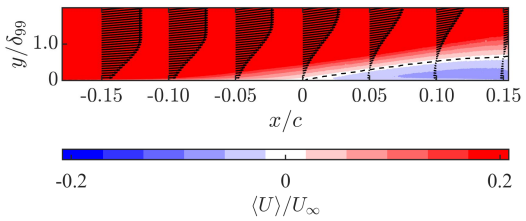

Figure 2. Mean velocity profile at various chordwise positions upstream and downstream of mean separation.

layer from the surface at $x/c = 0$, which is followed by a region of reversed flow.

The characteristics of the boundary layer is summarized in table 1. An increase of wall-normal velocity and a reduction of streamwise velocity is observed with downstream distance. The shape factor of the boundary layer (H) at $x/c = -0.15$ is 2.1, which means APG is evident even at the most upstream region of the FOV. At the mean separation point, the ratio $V_{\infty,x}/U_{\infty,x}$ is 0.14 compared to 0.18 as observed by Wadcock (1987). The discrepancy between the present result and that of Wadcock (1987) can be attributed to the fact that fluid can escape the APG in both the wall-normal and spanwise directions. As separation is approached, the boundary layer loses the fullness that is exhibited by a turbulent-boundary layer with ZPG. The change is highlighted by an increase of the shape factor with downstream distance and a value of $H = 3.6$ is reached at the detachment point. This value is similar to the shape factor obtained in existing studies of two-dimensional separation performed by Wadcock (1987), and Angele and Muhammad-Klingmann (2006).

Table 1. Boundary layer parameters for various positions upstream of separation.

x/c	$U_{\infty,x}$ [ms-1]	$V_{\infty,x}$ [m s-1]	δ_{99} [mm]	H
−0.15	12.83	1.21	26.3	2.1
−0.10	12.33	1.3	31.5	2.5
−0.05	12.1	1.49	37.8	2.9
0	11.89	1.69	45.5	3.6

MEAN SKIN-FRICTION LINES

The near-wall topology obtained from near-wall PIV is expected to be similar to the skin-friction lines if the measured plane is sufficiently close to the wall. Even if the measurement plane is not located within the linear viscous sublayer of the boundary layer, the measured velocity field can still be used to estimate the skin-friction lines with minor positional discrepancies (Depardon *et al.*, 2005). For separated flow around a cube, topological consistency is preserved when the measurement plane is located less than $0.12\delta_{99}$ from the surface. The critical value is likely dependent on the type of flow, but the separated flow featured in the investigation of Depardon *et al.* (2005) is more complex than the stall cell presented in this study (i.e. there are fewer singular points here). The measurement plane in the current study is located at $y = 2$ mm, equating to $0.06\delta_{99}$ where

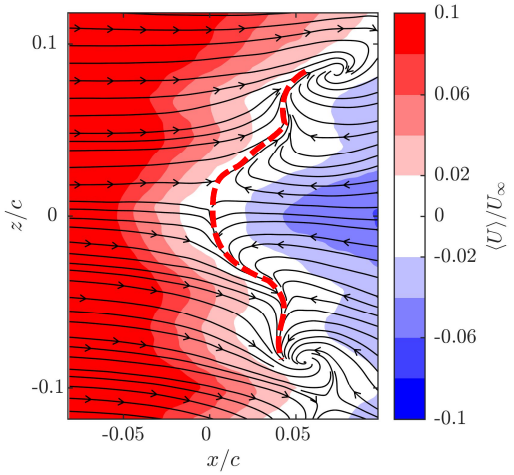

Figure 3. Streamlines of the mean near-surface ($y = 2$ mm) velocity field in vicinity of separation. The separation line branching from the saddle point at mid-span is shown by the dashed-line.

δ_{99} is the boundary layer thickness at the most upstream position in the FOV ($x/c = -0.15$). The PIV measurements are therefore expected to provide sufficient estimations of the skin-friction lines on the surface.

The near-surface streamlines are presented in figure 3 with normalized mean streamwise velocity shown in the background. Three-dimensional separation is evident since the skin-friction pattern contains a saddle point (Tobak and Peake, 1982) and the near-wall topology contains spanwise variation. Spanwise motion is present at both sides of the airfoil immediately upstream of the separation. This is explained by the tendency of flow to escape in the spanwise direction in the presence of an APG. The detachment-type separation line, highlighted by the dashed-line in figure 3, rolls into the foci and forms tornado-like vortices (Délery, 2001). This pattern is similar to the stall cells observed in the previous literature (Winkelmann and Barlow, 1980; Broeren and Bragg, 2001; Manolesos *et al.*, 2014).

The contours of the normalized Reynolds shear stress term ($\langle uw \rangle / U_\infty^2$) shown in figure 4 and reveal streamwise-elongated streaks of large shear stress magnitude. The regions of large shear stress near mid-span are located along the mean detachment lines emanating from the saddle point. The secondary regions of large shear stress at $z/c = \pm 0.08$ are located at the same spanwise position as the two counter-rotating foci. It is clear from figure 4 that the Reynolds shear stress varies along the span but less so in the streamwise direction. In other words, there is no additional increase in stress at the exact location of the saddle point and foci. The streaks are aligned with the section of the span where the flow profile possess the largest gradient ($\partial \langle U \rangle / \partial z$). This implies that the saddle point and foci do not create excess Reynolds shear stress, but are linked to the velocity gradient in the spanwise direction.

ENERGY SPECTRUM

A discrete Fourier transform (DFT) by the form of Welch's overlapping segment average was performed on both the fluctuating streamwise and spanwise velocity in time-resolved

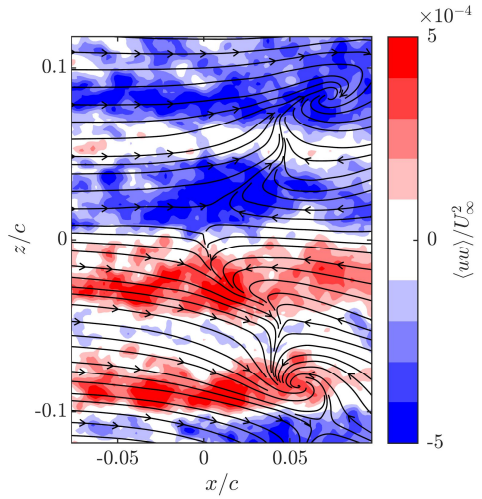

Figure 4. Contours of the normalized Reynolds shear stress ($\langle uw \rangle / U_\infty^2$) in the near-surface plane.

dataset of FOV2 to identify the frequencies present in the flow. Hanning windows were applied to segments with 50% overlap to maintain equal weighting among all data points. A segment length of 438 images, chosen iteratively, was used to eliminate noise in the spectral density, resulting in a frequency resolution of 4.0 Hz. The spectral density was evaluated for each set of time-resolved data and then averaged (five sets total). The power spectral density (PSD) of the fluctuating streamwise velocity is presented in figure 5(*a*) and the PSD of the fluctuating spanwise velocity is shown in figure 5(*b*). Three points of interest along the mid-span (z/c = 0) were selected: one upstream of the separation (x/c = −0.05), one at the saddle point (x/c = 0), and another within the region of reverse flow (x/c = 0.05). Spectral analysis of the fluctuating velocities at locations away from the mid-span were also investigated and yielded similar results as the ones shown here. As is evident in the plot, the flow at all three points is dominated by a low-frequency structure. There is also a gradual decrease in the amplitude of high-frequency components (>100 Hz) as the flow progressed downstream.

Zaman *et al.* (1989) conducted a study on the oscillation of flow around a stalled airfoil and concluded that bluff body vortex shedding appeared during deep stall at high angles-of-attack with a non-dimensionalized frequency of 0.2. At lower angles, the vortex shedding frequency was replaced with a normalized frequency in the range of St = 0.02−0.05. Similar low frequency phenomenon was observed in studies done by Yon and Katz (1998) and Broeren and Bragg (2001) for stalled airfoils at low angle-of-attack. Zaman *et al.* (1989) attributed this low frequency fluctuation to the transition of flow between a stall and unstalled state. The non-dimensionalized frequency is evaluated to be less than 0.05 in the present investigation, which is within the range of the oscillation described by Zaman's study.

INSTANTANEOUS FLOW

A sample snapshot of the instantaneous skin-friction lines is presented with contours of the normalized instantaneous streamwise velocity (U/U_∞) in figure 6(a) and Q criterion in figure 6(*b*). It is shown from the figures that the skin-friction lines become more chaotic as the near-surface flow changes

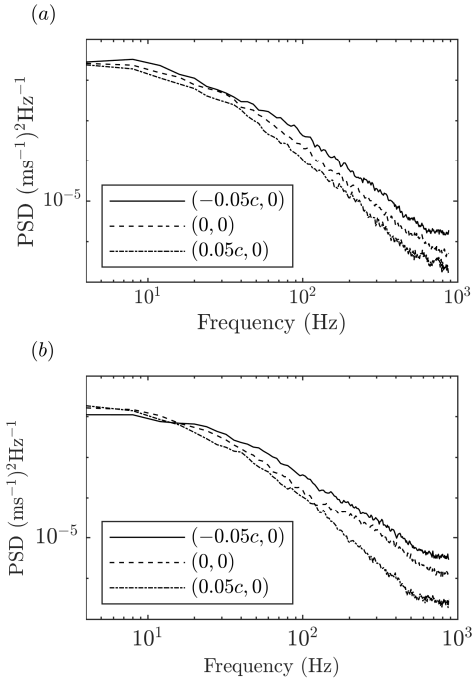

Figure 5. PSD of fluctuating velocity u and w at an upstream point, separation point, and a downstream point at mid-span.

from boundary layer flow to separated flow. The Q criterion along with the skin-friction lines in figure 6(*b*) are used to distinguish between turbulent vortices and separation structures (saddle points and foci). Separation structures still exist within the separation zone in the instantaneous snapshot, but are difficult to isolate since they are highly distorted by turbulent vortices and noise. At the same time, stall cell structures are not observed in the instantaneous skin-friction lines.

In order to remove the small-scale high frequency structures in the instantaneous snapshots, a moving average filter

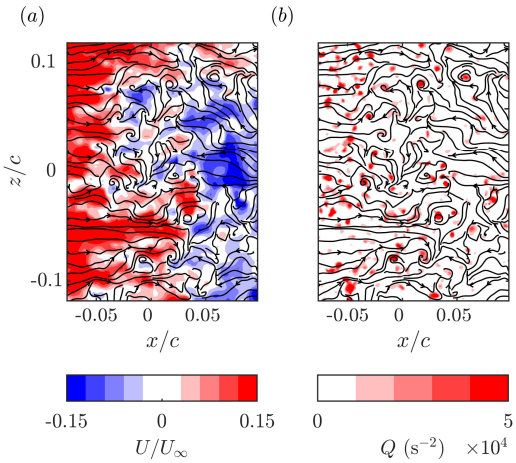

Figure 6. Streamlines of an instantaneous velocity field with (*a*) instantaneous streamwise velocity and (*b*) Q criterion.

with kernel size k = 200 snapshots was applied over the time-resolved data. The 200 snapshots spanned over 0.114 s for an imaging frequency of 1750 Hz. The moving average filter acted as a low-pass filter with a -3 dB cut-off frequency at St = 0.05. The filter will remove higher order oscillations while preserving the low-frequency motion shown in the spectral analysis and observed in past studies (Zaman *et al*., 1989; Broeren and Bragg, 2001). The sample instantaneous snapshot in figure 6 is filtered and shown in figure 7(*a*) with normalized instantaneous velocity and figure 7(*b*) with Q criterion. At first glance of the skin-friction lines, separation structures are more distinct within the separation region. Simultaneously, majority of small turbulent vortices have been filtered out of the snapshot. It is believed that there are no connection between separation structures and small-scale turbulent vortices, as saddle points and foci become prevalent after applying the filter.

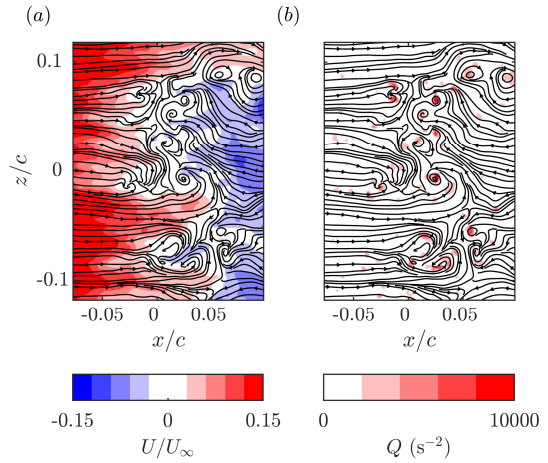

Figure 7. Streamlines of an instantaneous velocity field with (*a*) instantaneous streamwise velocity and (*b*) Q criterion after applying a moving average filter with k = 200.

LOW-FREQUENCY MOTIONS

Inspection of the time-resolved skin-friction lines suggests a connection between the formation of foci and regions of strong local flow. The visualizations show that foci tend to form near regions of strong local flow at the separation front where there is a strong shear layer. High shear region at the separation front is caused by the influx of streamwise momentum from high-speed streaks of the upstream boundary layer and backflow motions. Momentum is then swept away from the surface via tornado-like vortices.

The progression over time for a pair of foci caused by a strong local backflow is highlighted in figure 8. The subfigures contain a zoomed-in view of the structures with instantaneous streamwise velocity (U) plotted in the background. The local separation line is displayed by the dashed-line to highlight the movement of the local instantaneous separation line. Figure 8(*a*) shows a pair of foci beginning to form due an influx of momentum from the backflow region, as identified by the yellow arrow. After 0.079 s, the pair of foci shifts to the side of the streak where the shear is highest. The centres are located at approximately (x/c, z/c) = (0.01, -0.02) and

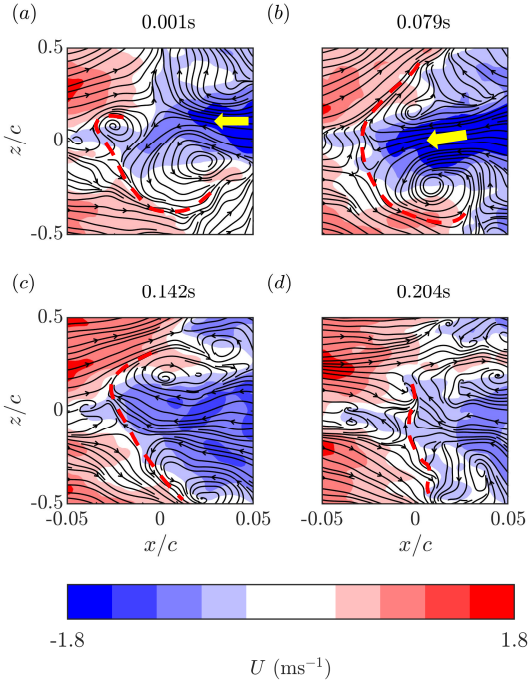

Figure 8. Formation of foci due to an influx of streamwise momentum from the backflow region.

(0, 0.01) in figure 8(*b*). As the incoming momentum subsides (figure 8(*c*)), the pair of foci eventually disintegrates and smaller unstable structures are left behind as shown in figure 8(*d*).

CONCLUSION

A PIV study of the near-wall streamlines showed a saddle point near mid-span and a pair of counter-rotating foci at the sides, which is reminiscent of a stall cell. The separated flow consisted largely of low-frequency structures. Saddle points and foci cannot be observed in the instantaneous skin-friction lines because they are distorted by smaller turbulent vortices. A low-pass filter of the sliding-average type was applied on the time-resolved data to isolate the low-frequency motions. By investigation of the time-resolved skin-friction lines, it was concluded that foci are formed at high-shear region created by an influx of momentum from high-speed streaks in the upstream flow or backflow region. The momentum is swept away from the surface via tornado-like vortices. The formation and destruction of foci contribute to the intermittency of the separation line. The lifespan of foci is likely directly proportional to duration and strength of the high-speed streaks.

REFERENCES

Angele, K. P., & Muhammad-Klingmann, B. PIV measurements in a weakly separating and reattaching turbulent boundary layer. *European Journal of Mechanics-B/Fluids*, 25.2. (2006): 204-222.

Broeren, A. P., & Bragg, M. B. Spanwise variation in the unsteady stalling flowfields of two-dimensional airfoil models. *AIAA journal*, 39.9. (2001): 1641-1651.

Délery, J. M. "Robert Legendre and Henri Werlé: toward the elucidation of three-dimensional separation." *Annual review of fluid mechanics* 33.1. (2001): 129-154.

Dell'Orso, H., & Amitay, M. Parametric investigation of stall cell formation on a NACA 0015 Airfoil. *AIAA Journal*, 56.8. (2018): 3216-3228.

Depardon, S., Lasserre, J. J., Boueilh, J. C., Brizzi, L. E., & Borée, J. Skin friction pattern analysis using near-wall PIV. *Experiments in Fluids*, 39.5. (2005): 805-818.

Ghaemi, S., Ragni, D., & Scarano, F. PIV-based pressure fluctuations in the turbulent boundary layer. *Experiments in fluids*, 53.6. (2012): 1823-1840.

Liu, T., Woodiga, S., & Ma, T. Skin friction topology in a region enclosed by penetrable boundary. *Experiments in fluids*, 51.6. (2011): 1549-1562.

Manolesos, M., & Voutsinas, S. G. Study of a stall cell using stereo particle image velocimetry. *Physics of Fluids*, 26.4. (2014): 045101.

Manolesos, M, Georgios P., and Voutsinas, S.G. "Experimental and computational analysis of stall cells on rectangular wings." *Wind Energy* 17.6. (2014): 939-955.

Meinhart, C. D., Wereley, S. T., & Santiago, J. G. A PIV algorithm for estimating time-averaged velocity fields. *Journal of Fluids Engineering*, 122.2. (2000): 285-289.

Tobak, M., & Peake, D. J. Topology of three-dimensional separated flows. *Annual review of fluid mechanics*, 14.1. (1982): 61-85.

Wadcock, A. J. Investigation of low-speed turbulent separated flow around airfoils. *NASA Contractor Report 177450* (1987).

Winkelmann, A.E., and Barlow, J.B. "Flowfield model for a rectangular planform wing beyond stall." *AIAA Journal* 18.8. (1989): 1006-1008.

Yon, S. A., & Katz, J. Study of the unsteady flow features on a stalled wing. *AIAA journal*, 36.3. (1998): 305-312.

Zaman, K. B. M. Q., McKinzie, D. J., & Rumsey, C. L. A natural low-frequency oscillation of the flow over an airfoil near stalling conditions. *Journal of Fluid Mechanics*, 202. (1989): 403-442.